DMC-ICE13: Ambient and high pressure polymorphs of ice from diffusion Monte Carlo and density functional theory (F)

(iD) **Flaviano Della Pia**, (iD) **Andrea Zen**, (iD) **Dario Alfè**, et al.

COLLECTIONS

(F)   This paper was selected as Featured

View Online   Export Citation   CrossMark

ARTICLES YOU MAY BE INTERESTED IN

`DMC-ICE13`: Ambient and high pressure polymorphs of ice from diffusion Monte Carlo and density functional theory

Flaviano Della Pia,[1] (iD) Andrea Zen,[2,3] (iD) Dario Alfè,[2,3,4,5] (iD) and Angelos Michaelides[1,a)] (iD)

AFFILIATIONS

[1] Yusuf Hamied Department of Chemistry, University of Cambridge, Cambridge CB2 1EW, United Kingdom
[2] Dipartimento di Fisica Ettore Pancini, Università di Napoli Federico II, Monte S. Angelo Napoli, I-80126, Italy
[3] Department of Earth Sciences, University College London, London WC1E 6BT, United Kingdom
[4] Thomas Young Centre, University College London, London WC1E 6BT, United Kingdom
[5] London Centre for Nanotechnology, University College London, London WC1E 6BT, United Kingdom

[a)] Author to whom correspondence should be addressed: am452@cam.ac.uk

ABSTRACT

Ice is one of the most important and interesting molecular crystals, exhibiting a rich and evolving phase diagram. Recent discoveries mean that there are now 20 distinct polymorphs; a structural diversity that arises from a delicate interplay of hydrogen bonding and van der Waals dispersion forces. This wealth of structures provides a stern test of electronic structure theories, with Density Functional Theory (DFT) often not able to accurately characterize the relative energies of the various ice polymorphs. Thanks to recent advances that enable the accurate and efficient treatment of molecular crystals with Diffusion Monte Carlo (DMC), we present here the `DMC-ICE13` dataset; a dataset of lattice energies of 13 ice polymorphs. This dataset encompasses the full structural complexity found in the ambient and high-pressure molecular ice polymorphs, and when experimental reference energies are available, our DMC results deliver sub-chemical accuracy. Using this dataset, we then perform an extensive benchmark of a broad range of DFT functionals. Of the functionals considered, revPBE-D3 and RSCAN reproduce reference absolute lattice energies with the smallest error, while optB86b-vdW and SCAN+rVV10 have the best performance on the relative lattice energies. Our results suggest that a single functional achieving reliable performance for all phases is still missing, and that care is needed in the selection of the most appropriate functional for the desired application. The insights obtained here may also be relevant to liquid water and other hydrogen-bonded and dispersion-bonded molecular crystals.

I. INTRODUCTION

Water and ice are ubiquitous in nature and relevant to an almost endless list of scientific problems in materials science, chemistry, physics, and biology. This broad interest has motivated many decades of research into the phase diagram of water and ice, with renewed interest in the last few years owing, for example, to the discovery of several new crystalline polymorphs,[1–5] and the theoretical prediction of numerous further candidates, e.g., Ref. 6. The recent experimental discoveries have increased the already extreme complexity of the water phase diagram to 20 solid phases, the liquid state, and various amorphous phases.[7–11] An accurate description of the phase diagram has been a major challenge for computational approaches, and excellent progress has been made both with classical potentials[12,13] and Machine Learning (ML) models.[14,15] The ML work has been particularly impressive, testing several Density Functional Theory (DFT) functionals (SCAN, B3LYP+D, PBE0+D, and revPBE0+D), as well as taking into account quantum nuclear effects (QNEs). However, differences between the computed and experimental phase boundaries still exist. Although thermal and QNEs are important, the key to the phase diagram is an accurate description of the relative energies of the various ice polymorphs. It is this issue that the present paper focuses on.

The main parameters used to assess the stability of ice polymorphs are the absolute lattice energy (i.e., the crystal total energy relative to gas phase water molecules) and the relative lattice energy (i.e., the lattice energy of a polymorph relative to hexagonal ice). Since the first DFT study of Hamann[16] in 1997, a large number of DFT studies (considering a broad range of exchange–correlation functionals) have followed (see, e.g., Refs. 17–23 and, for a review, see Ref. 24). Considerable insight has emerged from these studies, notably the realization that non-local van der Waals (vdW) dispersion forces need to be accounted for an accurate description of the relative energies of the different polymorphs. Generally, the above studies have made reference to benchmark lattice energies derived from Whalley's work.[25] Consequently, benchmark lattice energies are available only for polymorphs characterized before then. In the absence of experiment, high-level electronic structure theories can, in principle, provide an alternative source of benchmark reference data. And, indeed, the energetics of several ice polymorphs have been examined with various explicitly correlated electronic structure theories.[26–29] In particular, Diffusion Monte Carlo (DMC) gives excellent results in the computation of water-ice lattice energies.[18,26,30] However, largely because of the computational cost of DMC, estimates are only available for four polymorphs (ice Ih, II, VIII, and XI).

In this study, thanks to recent developments[31,32] enabling accurate and efficient DMC simulations for molecular crystals,[26] we perform an extensive DMC study of ice polymorphs. High-accuracy reference values of the lattice energy for 13 ice polymorphs are provided, with the 13 polymorphs selected to provide a broad treatment of the main bonding topologies found in the ambient and high-pressure molecular ice polymorphs. We subsequently use the DMC reference energies to conduct a benchmark on a broad range of DFT exchange–correlation (XC) functionals. This reveals that different functionals perform better in capturing the stability with respect to the gas or the solid phase, indicating that care should be taken in selecting the optimal functional for a particular study. From another perspective, our results suggest that a "universal" functional for water, i.e., a functional that gives a good agreement for all phases, is still missing.

The outline of this paper is as follows: In Sec. II, we introduce the 13 ice polymorphs under consideration and then give technical details of both DFT and DMC simulations. In Sec. III, we first present the DMC reference values, comparing with available experimental results. Subsequently, we present the outcome of the benchmark of numerous DFT-XC functionals, analyzing the stability of the considered polymorphs with respect to the gas phase and hexagonal ice. Finally, we give some concluding remarks in Sec. IV.

II. MATERIALS AND METHODS

A. Dataset setup

In this work, we compiled the `DMC-ICE13` set by considering 13 ice polymorphs, including hydrogen-ordered and -disordered phases that span a broad range of temperatures and pressures on the water phase diagram.[11] First, we considered the structures previously included in the DFT database `ICE10`[21] — ice Ih, II, III, VI, VII, VIII, IX, XIII, XIV, and XV. Then, we added the ordered counterpart of hexagonal ice, ice XI, leaving out the cubic ice Ic, expected to be isoenergetic with ice XI/Ih within the DMC statistical error.[30]

Finally, we considered the meta-stable and self-interpenetrating structure of ice IV and the recently discovered ice XVII.[3] Interestingly, this is an ultra-low-density porous state and has its stability domain in the negative pressure regions; however, it is meta-stable at ambient pressures and low temperatures. In this way, we are taking into account at least one polymorph for each hydrogen ordered-disordered couple (both for ice XI/Ih, VIII/VII, IX/III, and XV/VI). We leave out of the set ice XII and V, disordered counterparts of ice XIV and XIII, respectively. Finally, we do not include the least dense ice XVI, stable only at negative pressures, ice XIX, described as the "glassy" counterpart of ice VI, and the high pressures symmetric ice X, and "superionic water" ice XVIII. In fact, these phases go beyond the intent of this study, which is focused on molecular crystals.

We note here that, in principle, several structures should be considered when computing the lattice energy of hydrogen-disordered polymorphs. Based on a DFT analysis reported in the supplementary material, we estimate that the differences among the lattice energies of different hydrogen arrangements are of the order of the DMC error bars. Being indistinguishable at the DMC level, we consider only one hydrogen arrangement for each hydrogen-disordered phase.

The geometries of the considered structures are reported in the supplementary material and shown in Fig. 1. Input DFT and DMC files are provided as supplementary material, to facilitate accessibility and reproducibility of our data.

B. Geometry optimization and DFT lattice energies

The physical quantity usually considered to establish the stability of a crystal is its absolute lattice energy, which is the energy per molecule gained upon assuming the crystal form with respect to the gas phase. It can be computed as

$$E_{\text{latt}} = E_{\text{crys}} - E_{\text{gas}}, \tag{1}$$

where E_{crys} is the energy per molecule in the crystal phase, and E_{gas} is the energy of the isolated molecule. However, we are also interested in capturing the relative stability of the ice polymorphs, i.e., the stability with respect to a fixed crystalline phase instead of the gas state. This property is more relevant in, e.g., the computation of the water phase diagram. Therefore, we assess the relative stability of the crystalline phases by computing the relative lattice energy with respect to hexagonal ice Ih. For a general polymorph "x," this is simply computed as

$$\Delta E_{\text{latt}}^{x} = E_{\text{latt}}^{x} - E_{\text{latt}}^{\text{Ih}} \tag{2}$$

and is independent of the configuration of the monomer in the gas phase.

Initial structures of ice Ih, II, VIII, XIII, XIV, and XV were taken from Ref. 18, ice III, VI, VII, IX, and XVII were taken from Ref. 6, ice IV was taken from Ref. 34, and ice XI from Ref. 30. DFT calculations have been performed with the VASP program package.[35–38] The projector-augmented plane wave method (PAW) has been used with hard pseudo-potentials,[39,40] with a dense FFT grid and a PAW energy cut-off of 1000 eV, necessary to achieve convergence in unconstrained geometry optimization, as reported in Ref. 21. To be consistent in the benchmark of several exchange–correlation functionals with respect to the reference
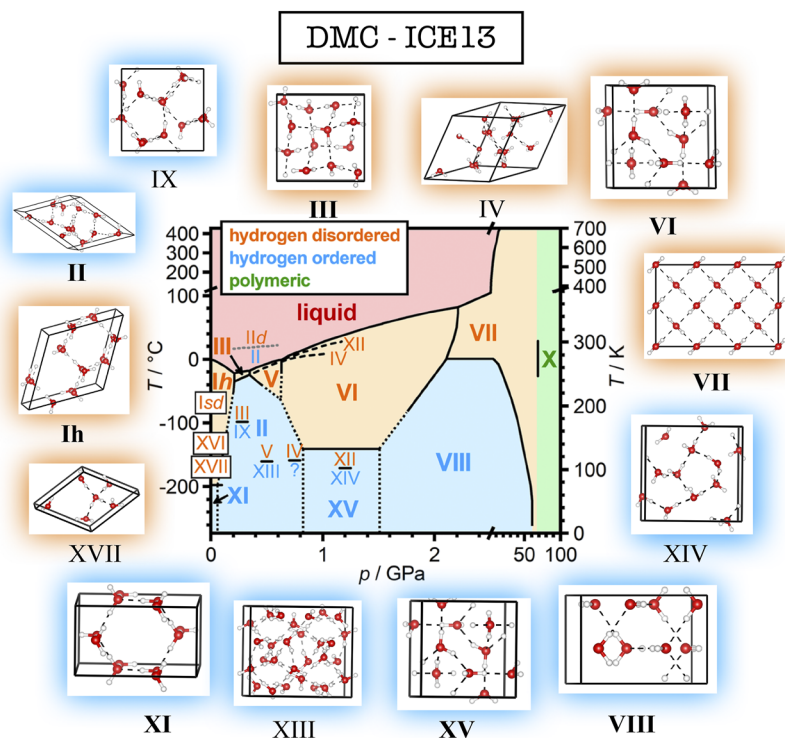
FIG. 1. Crystalline structures of the systems contained in the DMC−ICE13 dataset. Each subplot reports the unit cell of the specified polymorph (plotted using VESTA[33]), with oxygen atoms in red, hydrogen atoms in white, and hydrogen bonds as dashed black lines. The experimental phase diagram published in Ref. 11 is reported here to facilitate visualization of the phase diagram regions covered by our dataset. Adopting the convention of Ref. 11, stable phases are indicated by large bold Roman numerals, whereas meta-stable states are indicated by a smaller font size. The phase diagram is reproduced from C. G. Salzmann, J. Chem. Phys. 150, 060901 (2019) with the permission of AIP Publishing.

(DMC) value computed on a fixed geometry, we relaxed all the ice polymorph structures at a fixed DFT-XC level. These structures have therefore been used both in the DMC and DFT evaluations of the lattice energies. This is the standard procedure also adopted in previous benchmarks.[18,19,21]

Since the previous DMC calculations on ice Ih, II, and VIII with PBE structures have shown results in excellent agreement with experimental values,[18,26] we decided to optimize the geometry of all the considered polymorphs with the PBE functional; the potential error due to this approximation is estimated to be smaller than ~1 kJ/mol, as discussed in the supplementary material. All geometries have been carefully optimized until all forces were less than ~0.002 eV/Å, sampling the Brillouin zone with a $3 \times 3 \times 3$ **k**-point grid centred on the Γ point. The convergence of the structure relaxation for several polymorphs has been subsequently checked using a denser $5 \times 5 \times 5$ grid. A $3 \times 3 \times 3$ **k**-point grid has been used to perform GGAs, *meta*-GGAs, and vdW-inclusive single-point periodic calculations, yielding a 1 meV convergence threshold on the lattice energy, evaluated with respect to the $5 \times 5 \times 5$ grid. A denser $4 \times 4 \times 4$ **k**-point grid has been used for hybrid-XC calculations to achieve the same accuracy. The geometry used for the isolated molecule (gas phase) can also influence the value of E_{latt} [see Eq. (1)]. For this, we used the most accurate geometry for the water monomer, derived by Partridge and Schwenke[41] using coupled cluster with single, double and perturbative triple excitations [CCSD(T)], which is already used in previous analyzes.[18,26,42] An additional DMC calculation has been performed for the computation of E_{gas} on the water monomer geometry optimized at the DFT-PBE level, leading to a variation in the absolute lattice energies smaller than 1 kJ/mol.

There are now countless DFT functionals and we cannot test all or even most of them. Rather, here, we focus on evaluating the performance of some of the most widely used families of functionals for water and ice. Specifically, we considered local-density approximation (LDA),[43] GGA (PBE,[44] revPBE[45]), several dispersion-inclusive functionals (optB88-vdW,[46] optB86-vdW,[47] optPBE-vdW,[46] vdW-DF,[48] vdW-DF2,[49] rev-vdW-DF2[50]), *meta*-GGA (SCAN,[51] RSCAN,[52] R2SCAN,[53] SCAN+rVV10[54]), and hybrid methods (PBE0,[55,56] revPBE0,[57] B3LYP[58,59]). GGA and hybrid methods have also been applied with the D3—with both zero and Becke–Johnson (BJ) damping, and with or without the three-body dispersion term of Axilrod–Teller–Muto (ATM)—and D4 London dispersion correction using the dftd3/dftd4[60–64] tools. PBE and PBE0 have also been evaluated with the Tkatchenko–Scheffler (TS) dispersion correction[65] and the Many-Body-Dispersion (MBD) method.[66,67] We also tested the Hartree–Fock (HF) approach.

C. Diffusion Monte Carlo

Reference values for the lattice energies were computed with fixed-node DMC (FN-DMC) by using the CASINO code.[68] We used Hartree–Fock pseudo-potentials[69,70] with the most recent determinant locality approximation (DLA).[32] The trial wave-functions were of the Slater–Jastrow type with single Slater determinants, and the single-particle orbitals obtained from DFT local-density approximation (LDA) plane-wave calculations performed with PWscf[71,72] by using an energy cut-off of 600 Ry and re-expanded in terms of B-splines.[73] The Jastrow factor included a two-body electron–electron (e–e) term, two-body electron–nucleus (e–n) terms, and three-body

electron–electron–nucleus (e–e–n) terms. The variational parameters of the Jastrow have been optimized by minimizing the variance in the simulated cell for each analyzed polymorph. The size of the simulation cell imposes some constraints on the Jastrow variational freedom, in the form of cut-offs in the e–n, e–e and e–e–n terms. Following the workflow given in Ref. 26, tested on several molecular crystals including three ice polymorphs, the simulation cells have been generally defined in order to guarantee the radius of the sphere inscribed in the Wigner–Seitz cell to be greater than 5 Å. The number of molecules in the simulated cell of each polymorph is reported in the supplementary material.

The time step τ is a key issue affecting the accuracy of DMC calculations. In DMC, a propagation according to the imaginary time Schrödinger equation is performed to project out the exact ground state from a trial wave-function.[74] A time step τ must be chosen, but the projection is exact only in the continuous limit $\tau \to 0$. However, the ZSGMA[31] DMC algorithm gives better convergence with respect to τ than previously used methods because the time-step bias per molecule is independent of the size of the simulated cell in a molecular crystal.[26] In this work, we have verified the time-step convergence for each analyzed ice polymorph, as reported in the supplementary material. We note that, in general, even in the limit of zero-time step, the DMC energy may be biased by the choice of the Jastrow factor, depending on how the non-local part of the pseudo-potential is treated. This bias is eliminated if the DLA scheme is employed.

The computation of E_{crys} involves the use of periodic boundary conditions that can be subject to significant finite size errors (FSE). We took into account FSE using the Model Periodic Coulomb (MPC)[75–77] correction and further correct for the (smaller) Independent Particle FSE (IPFSE) according to the procedure described in Ref. 26. An analysis of the FSE for each considered polymorph can be found in the supplementary material.

Finally, the periodic DMC simulations have been performed by using Twist Averaging Boundary Condition (TABC).[78] This involves averaging the absolute DMC energies obtained by using DFT-LDA single Slater determinants computed at different $\mathbf{k}$-points in the Brillouin zone of the simulated cell. In particular, this means that the general DMC wave function of a periodic system is a complex function, except for a finite set of points in the Brillouin zone that makes the wave function real, such as the Γ point or the corner points. In this case, the FN-DMC is substituted by the non-equivalent fixed-phase DMC (FP-DMC). In principle, this means that E_{gas} also has to be computed with the FP-DMC, in order to be consistent in the estimation of E_{latt}. However, it has been shown in Ref. 26 that the difference between the FN and FP estimates of E_{gas} for water is smaller than the statistical accuracy. For this reason, we used a real wave function in the DMC simulation of the gas phase.

III. RESULTS AND DISCUSSION

The computation of the lattice energy is performed at zero temperature and pressure and considering only the electronic contribution, i.e., neglecting quantum nuclear effects. Experimental estimates of the ice polymorphs lattice energies have been deducted from measures of the internal energy variation, according to an approximation described in the supplementary material. These experimental values are affected by two types of error: an uncertainty coming from the actual measurement of the internal energy variation (~0.1 kJ/mol),

and an error due to the correction for the zero-point energy effects that we estimate to be of the order of ~1 – 2 kJ/mol, as generally found for molecular crystals in Ref. 26, and further analyzed for ice polymorphs in the supplementary material. This uncertainty on the experimental estimates of the lattice energies and the lack of them for the recently discovered phases are key reasons why results from a high-accuracy electronic structure method, such as DMC, are needed.

In Fig. 2, we report the DMC estimates, as well as the experimental values when available, of both the absolute (top panel) and relative (bottom panel) lattice energies for all the considered polymorphs. Exact values are also reported in Table I. First, we note that our DMC values for ice Ih and II agree within statistical error with the previous DMC results reported in Ref. 26. For ice VIII, a small (~1.5 kJ/mol) difference is found, which arises from the use, in the current study, of a bigger supercell and of the DLA in the pseudo-potentials (see Sec. II).

Recently, high-accuracy Random Phase Approximation with exchange (RPAx)[28] lattice energies were computed for several crystalline systems, including ice II, VIII, IX, and XI. We find our DMC estimates in good agreement with the reported values, with a maximum discrepancy of ~1.2 kJ/mol that can be mainly ascribed to the different functional (PBE+TS) used for the geometry optimization.

Observing the entire dataset, it is evident that the energy differences we want to catch in this work are minimal; in fact, they are, in
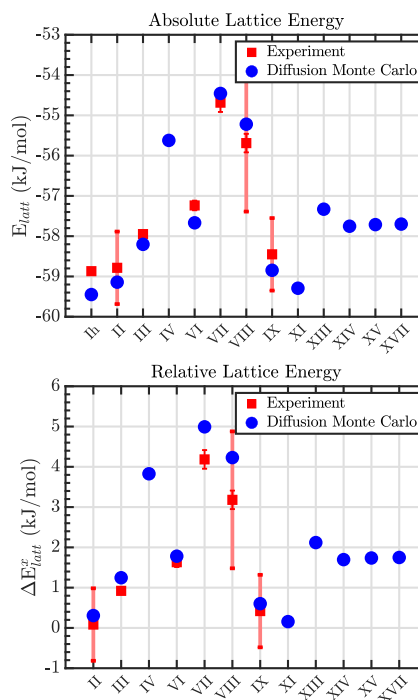
FIG. 2. Performance of DMC for the 13 ice polymorphs considered on the absolute (top) and relative (bottom) lattice energy, compared with available experimental data.[25] The error on the experimental estimates due to the correction for the zero-point energy, estimated in the supplementary material, is reported with a shaded error bar for ice II, VIII, and IX. Energies are given in kJ/mol.

TABLE I. Experimental (Ref. 25) and DMC values (errors given in parentheses) for the absolute and relative lattice energies. Energies are in kJ/mol. [n.a. ≡ not available].

Polymorph	Absolute Lattice Energy		Relative Lattice Energy	
	EXP	DMC	EXP	DMC
Ih	−58.87(1)	−59.45(7)	⋯	⋯
II	−58.78(10)	−59.14(7)	0.08(10)	0.31(10)
III	−57.95(5)	−58.20(7)	0.92(5)	1.25(10)
IV	n.a.	−55.62(7)	n.a.	3.83(10)
VI	−57.24(12)	−57.67(7)	1.63(12)	1.78(10)
VII	−54.68(23)	−54.46(7)	4.18(23)	4.99(10)
VIII	−55.69(23)	−55.22(8)	3.18(23)	4.23(10)
IX	−58.45(8)	−58.85(7)	0.42(8)	0.60(10)
XI	n.a.	−59.29(8)	n.a.	0.15(10)
XIII	n.a.	−57.33(7)	n.a.	2.12(10)
XIV	n.a.	−57.75(7)	n.a.	1.70(10)
XV	n.a.	−57.71(7)	n.a.	1.74(10)
XVII	n.a.	−57.70(8)	n.a.	1.75(10)

most cases, smaller than the "chemical accuracy" limit of 4 kJ/mol. In particular, ice XIV, XV, and XVII are degenerate within the DMC statistical error. Overall, all the lattice energies vary in a small range of 5 kJ/mol, defined by the lowest pressure phase ice Ih/XI and the highest pressure phase ice VII. Interestingly, we find that all the "recent" polymorphs, where no experimental value is available, fall in this range. Overall, DMC is always in good agreement with the experimental values, with a maximum disagreement of 0.5 kJ/mol on the absolute lattice energies, and ~1 kJ/mol on the relative lattice energies. Thus, it ultimately defines the reference method we use to establish the performance of the DFT functionals.

The benchmark of several DFT methods has been conducted by dividing the XC functionals in macro-classes, reported roughly according to Jacob's ladder, as GGA, vdW-inclusive functionals, *meta*-GGA, and hybrid functionals. Also, HF was added to the benchmark. The HF, GGA, and hybrid dispersion-less functionals have been corrected through the D3/D4 correction, while the Tkatchenko–Scheffler (TS) and the Many-Body-Dispersion (MBD) corrections have also been taken into account for PBE and PBE0.

The absolute lattice energies are reported in Table II (we also include LDA lattice energies for completeness, but we leave them out of the general discussion since they are known to be unreliable). The performance of each functional is evaluated as the Mean Absolute Error (MAE) with respect to the reference DMC value, graphically reported both for the absolute and relative lattice energies in Fig. 3 to allow for easier comparisons. In particular, in the following analysis, XC functionals are generally classified as "good," if their MAE is ≲4 kJ/mol (≲2 kJ/mol) for the absolute (relative) lattice energy.

Overall, as expected, the worst performance on the absolute lattice energy is obtained at the HF level, with significant improvement (>50%) gained, thanks to the dispersion correction. Except for PBE, the performance of all functionals is improved by the *a posteriori* vdW correction. Interestingly, the performance on the relative lattice energies is significantly different. Remarkably, the HF method

performs better than several DFT functionals; however, its performance is significantly worsened by both D3 and D4 corrections. Unreliable results are generally achieved by both PBE and PBE0 regardless of the D3/D4 corrections. Overall, the only macro-classes where all the functionals achieve general good performance (on both the absolute and relative lattice energies) are the *meta*-GGAs and the vdW-inclusive functionals. As noted before, the energy differences between the considered polymorphs vary in a small range of 5 kJ/mol. For this reason, even if a functional generally achieves small errors in reproducing the reference DMC values for the absolute lattice energy, a fundamental condition to achieve good results on the relative lattice energy is a constant error among all the polymorphs, so that an error cancelation serves to yield the desired performance.

The best performing functionals for each XC macro-class are further analyzed in Fig. 4. In Fig. 4 (top), we focus on the absolute lattice energy. Among the considered *meta*-GGAs, only RSCAN and R2SCAN achieve particularly good results (MAE ~ 1 kJ/mol), while SCAN and SCAN+rVV10 have an MAE ~ 4 kJ/mol and ~10 kJ/mol, respectively. Several properties of liquid water have been shown to be correctly predicted by SCAN.[14,79,80] Its performance on a subset of six proton-ordered polymorphs (ice IX, II, XIII, XIV, XV, and VIII) has been previously analyzed by Sun *et al.*[22] They showed that SCAN reproduces relative lattice energies better than PBE, PBE0, and PBE0+TS. These considerations are confirmed by our dataset; however, we find several other XC functionals that achieve better performance. Good results are achieved by revPBE-D3 (almost equivalent with or without the Axilrod–Teller–Muto correction) and vdW-DF2, with their MAE being lower than 1.4 kJ/mol. However, as evident in both Fig. 4 and Table II, their error with respect to the DMC reference oscillates among all the polymorphs, leading to worse performance on the stability with respect to hexagonal ice. In Fig. 4 (bottom), we focus on the best performing functionals on the relative lattice energies, i.e., revPBE-D3 (GGA), optB86b-vdW (vdW-inclusive), SCAN+rVV10 (*meta*-GGA), and B3LYP-D3^{atm} (hybrid). Except for revPBE-D3, these functionals generally achieve poor performance when predicting the stability with respect to the gas phase, with an MAE of ~5 kJ/mol for B3LYP-D3^{atm} and even greater for optB86b-vdW (~7 kJ/mol) and SCAN+rVV10 (~10 kJ/mol). However, as suggested before, this error behaves like a constant offset with respect to DMC, with the error cancelation allowing for optimal predictions on the relative lattice energy.

Note, also, that the performance of B3LYP-D3, B3LYP-D3^{atm}, optB86b-vdW, and SCAN+rVV10 on the relative lattice energies is all equivalent within the statistical error of the DMC estimates (MAE between 0.5 and 0.7 kJ/mol). However, hybrid functional calculations require computational resources hundreds of times greater than *meta*-GGA and vdW-inclusive methods (and a denser **k**-point grid is necessary to achieve convergence). Therefore, we suggest the latter to obtain optimal results at a reasonable cost.

Remarkably, the DMC reference values allow us to qualitatively understand why ice III is only meta-stable in the recent computational phase diagrams.[14,15] Since we did not include ice V in our benchmark, we consider its ordered counterpart ice XIII in the following analysis. Neglecting the temperature contribution and the zero-point motion, and considering the zero pressure volumes, the

TABLE II. Performance of each exchange–correlation functional on the absolute lattice energy. Energies are reported in kJ/mol. In order to facilitate reproducibility in the supplementary material, we report the same table with energies in meV, directly comparable to the VASP output.

Method	Ih	II	III	IV	VI	VII	VIII	IX	XI	XIII	XIV	XV	XVII	MAE
DMC	−59.45	−59.14	−58.20	−55.62	−57.67	−54.46	−55.22	−58.85	−59.29	−57.33	−57.75	−57.71	−57.70	
B3LYP-D4	−63.03	−61.11	−60.42	−58.10	−58.69	−53.78	−54.98	−61.33	−63.20	−60.18	−59.60	−58.65	−62.05	2.20
B3LYP-D3(BJ)^{atm}	−63.63	−61.90	−61.11	−58.90	−59.60	−54.96	−56.21	−62.03	−63.80	−61.00	−60.43	−59.56	−62.68	2.88
B3LYP-D3(BJ)	−64.04	−62.52	−61.65	−59.57	−60.37	−55.86	−57.09	−62.62	−64.23	−61.68	−61.17	−60.31	−63.01	3.52
B3LYP-D3^{atm}	−64.14	−64.02	−62.10	−60.89	−62.24	−59.89	−60.95	−63.39	−64.28	−62.99	−62.61	−62.16	−63.24	4.96
B3LYP-D3	−64.55	−64.65	−62.64	−61.56	−63.01	−60.78	−61.84	−63.98	−64.71	−63.67	−63.34	−62.91	−63.57	5.60
B3LYP	−52.71	−46.96	−48.22	−43.85	−42.88	−35.97	−37.36	−48.49	−52.73	−45.72	−44.46	−43.03	−52.09	11.84
revPBE0-D4	−56.31	−54.00	−53.65	−51.17	−51.58	−46.87	−48.09	−54.41	−56.42	−53.05	−52.44	−51.62	−55.27	4.89
revPBE0-D3(BJ)^{atm}	−56.94	−55.02	−54.50	−52.22	−52.84	−48.38	−49.66	−55.32	−57.06	−54.15	−53.58	−52.86	−55.89	3.84
revPBE0-D3(BJ)	−57.35	−55.65	−55.04	−52.89	−53.60	−49.28	−50.55	−55.91	−57.48	−54.83	−54.32	−53.61	−56.22	3.21
revPBE0-D3^{atm}	−57.03	−56.96	−54.81	−53.80	−55.43	−54.71	−55.78	−56.03	−57.09	−55.65	−55.34	−55.40	−56.11	1.99
revPBE0-D3	−57.45	−57.58	−55.35	−54.47	−56.20	−55.61	−56.67	−56.61	−57.51	−56.33	−56.08	−56.15	−56.44	1.63
revPBE0	−44.05	−37.58	−39.51	−34.72	−33.31	−25.88	−27.35	−39.63	−44.00	−36.41	−35.03	−33.58	−43.29	21.08
PBE0-MBD	−65.15	−63.08	−62.56	−60.11	−60.74	−55.92	−57.14	−63.40	−65.42	−62.18	−61.54	−60.64	−64.11	4.12
PBE0-TS	−64.67	−64.14	−62.66	−61.30	−62.52	−41.88	−58.46	−63.76	−64.95	−63.44	−63.13	−62.43	−63.62	5.67
PBE0-D4	−64.38	−61.43	−61.48	−58.49	−58.75	−53.32	−54.56	−62.12	−64.63	−60.48	−59.74	−58.70	−63.34	2.82
PBE0-D3(BJ)^{atm}	−64.68	−61.80	−61.81	−58.87	−59.17	−53.88	−55.14	−62.45	−64.93	−60.86	−60.13	−59.12	−63.66	3.03
PBE0-D3(BJ)	−65.09	−62.42	−62.35	−59.54	−59.94	−54.78	−56.02	−63.03	−65.35	−61.54	−60.86	−59.87	−63.99	3.57
PBE0-D3^{atm}	−65.80	−64.77	−63.44	−61.18	−61.90	−57.85	−58.99	−64.35	−66.05	−63.22	−62.62	−61.82	−64.81	5.26
PBE0-D3	−66.21	−64.77	−63.98	−61.85	−62.67	−58.75	−59.88	−64.94	−66.47	−63.91	−63.35	−62.57	−65.14	5.85
PBE0	−57.47	−52.12	−53.27	−49.05	−48.39	−41.88	−43.23	−53.49	−57.63	−50.88	−49.74	−48.45	−56.77	6.62
SCAN + rVV10	−68.53	−68.31	−66.79	−65.65	−67.21	−64.88	−66.04	−67.56	−68.96	−67.55	−67.46	−66.99	−67.60	9.71
R2SCAN	−61.43	−59.94	−58.99	−57.20	−58.13	−54.98	−56.21	−59.59	−61.68	−59.00	−58.64	−58.02	−60.70	1.32
RSCAN	−61.36	−59.34	−58.63	−56.48	−57.32	−53.80	−55.01	−59.11	−61.65	−58.31	−57.87	−57.18	−60.72	0.95
SCAN	−64.70	−63.15	−62.23	−60.36	−61.35	−58.21	−59.42	−62.77	−65.06	−62.19	−61.84	−61.21	−64.00	4.55
optB88-vdW	−67.90	−67.85	−66.91	−65.66	−66.99	−63.50	−64.61	−67.88	−68.32	−67.66	−67.52	−66.82	−66.40	9.33
optB86b-vdW	−68.69	−67.89	−67.47	−65.74	−66.83	−62.84	−63.93	−68.22	−69.18	−67.68	−67.43	−66.63	−67.21	7.05
optPBE-vdW	−65.55	−65.72	−64.79	−63.77	−64.84	−61.25	−62.46	−65.93	−65.82	−65.66	−65.50	−64.83	−63.87	9.20
rev-vdW-DF2	−66.38	−64.26	−64.27	−61.87	−62.52	−57.90	−59.03	−64.84	−66.84	−63.79	−63.32	−62.35	−65.26	5.71
vdW-DF2	−59.43	−60.16	−58.40	−57.93	−59.18	−56.49	−57.80	−59.87	−59.43	−59.92	−59.84	−59.30	−58.06	1.34
vdW-DF	−53.59	−53.78	−52.86	−52.03	−52.74	−49.13	−50.47	−54.19	−53.59	−53.81	−53.60	−52.96	−51.84	4.91
revPBE-D4	−59.96	−56.47	−57.12	−54.00	−53.97	−48.67	−49.73	−57.33	−60.29	−55.68	−54.98	−53.90	−58.96	2.53
revPBE-D3(BJ)^{atm}	−58.86	−55.92	−56.39	−53.54	−53.66	−48.25	−49.43	−56.74	−59.17	−55.31	−54.64	−53.62	−57.80	2.71
revPBE-D3(BJ)	−59.27	−56.55	−56.92	−54.21	−54.42	−49.15	−50.31	−57.33	−59.59	−55.99	−55.37	−54.38	−58.13	2.17
revPBE-D3^{atm}	−58.60	−57.13	−56.15	−54.37	−55.40	−53.93	−54.85	−56.82	−58.83	−56.02	−55.57	−55.31	−57.68	1.36
revPBE-D3	−59.01	−57.75	−56.69	−55.03	−56.16	−54.83	−55.74	−57.41	−59.25	−56.71	−56.30	−56.07	−58.00	0.91
revPBE	−43.86	−35.59	−38.96	−33.16	−30.88	−21.89	−23.30	−38.52	−43.97	−34.66	−33.02	−31.14	−43.11	22.79
PBE-MBD	−70.48	−67.29	−67.77	−64.69	−64.75	−58.87	−59.94	−68.13	−70.96	−66.64	−65.83	−64.57	−69.40	8.53
PBE-TS	−69.59	−67.75	−67.44	−65.29	−65.86	−58.84	−60.36	−68.04	−70.10	−67.30	−66.81	−65.71	−68.53	8.71
PBE-D4	−69.62	−65.55	−66.60	−62.97	−62.71	−56.21	−57.35	−66.75	−70.10	−64.82	−63.96	−62.58	−68.61	6.88
PBE-D3(BJ)^{atm}	−69.95	−65.95	−66.96	−63.38	−63.19	−56.85	−58.02	−67.11	−70.43	−65.23	−64.38	−63.05	−68.96	7.31
PBE-D3(BJ)	−70.36	−66.58	−67.49	−64.05	−63.96	−57.75	−58.90	−67.69	−70.85	−65.92	−65.11	−63.80	−69.29	7.95
PBE-D3^{atm}	−70.39	−67.75	−67.94	−65.15	−65.41	−59.76	−60.90	−68.38	−70.87	−67.07	−66.37	−65.25	−69.42	8.94
PBE-D3	−70.80	−68.37	−68.47	−65.82	−66.17	−60.66	−61.79	−68.97	−71.29	−67.76	−67.11	−66.00	−69.75	9.58
PBE	−62.23	−55.54	−57.85	−52.85	−51.58	−43.79	−45.05	−57.56	−62.60	−54.54	−53.24	−51.56	−61.52	4.48
HF-D4	−42.89	−46.50	−41.70	−42.92	−45.69	−46.31	−47.99	−44.36	−42.18	−45.14	−45.47	−46.08	−41.82	13.03
HF-D3(BJ)^{atm}	−50.53	−53.57	−49.36	−50.04	−53.03	−53.70	−55.15	−51.58	−49.97	−52.28	−52.77	−53.25	−49.53	5.67
HF-D3(BJ)	−50.94	−54.20	−49.90	−50.70	−53.79	−54.60	−56.03	−52.16	−50.39	−52.97	−53.50	−54.00	−49.86	5.17
HF-D3^{atm}	−39.07	−44.94	−38.65	−41.32	−44.88	−47.30	−49.09	−41.88	−38.27	−43.58	−44.14	−45.31	−38.01	14.76
HF-D3	−39.49	−45.57	−39.19	−41.99	−45.64	−48.20	−49.97	−42.47	−38.69	−44.27	−44.88	−46.06	−38.34	14.13
HF	−26.57	−25.53	−23.38	−22.01	−22.58	−19.54	−21.57	−25.42	−25.62	−24.06	−23.47	−23.29	−25.73	33.82
LDA	−100.08	−94.37	−95.92	−90.94	−91.03	−83.78	−84.66	−95.37	−101.22	−93.04	−91.99	−90.32	−99.67	35.69
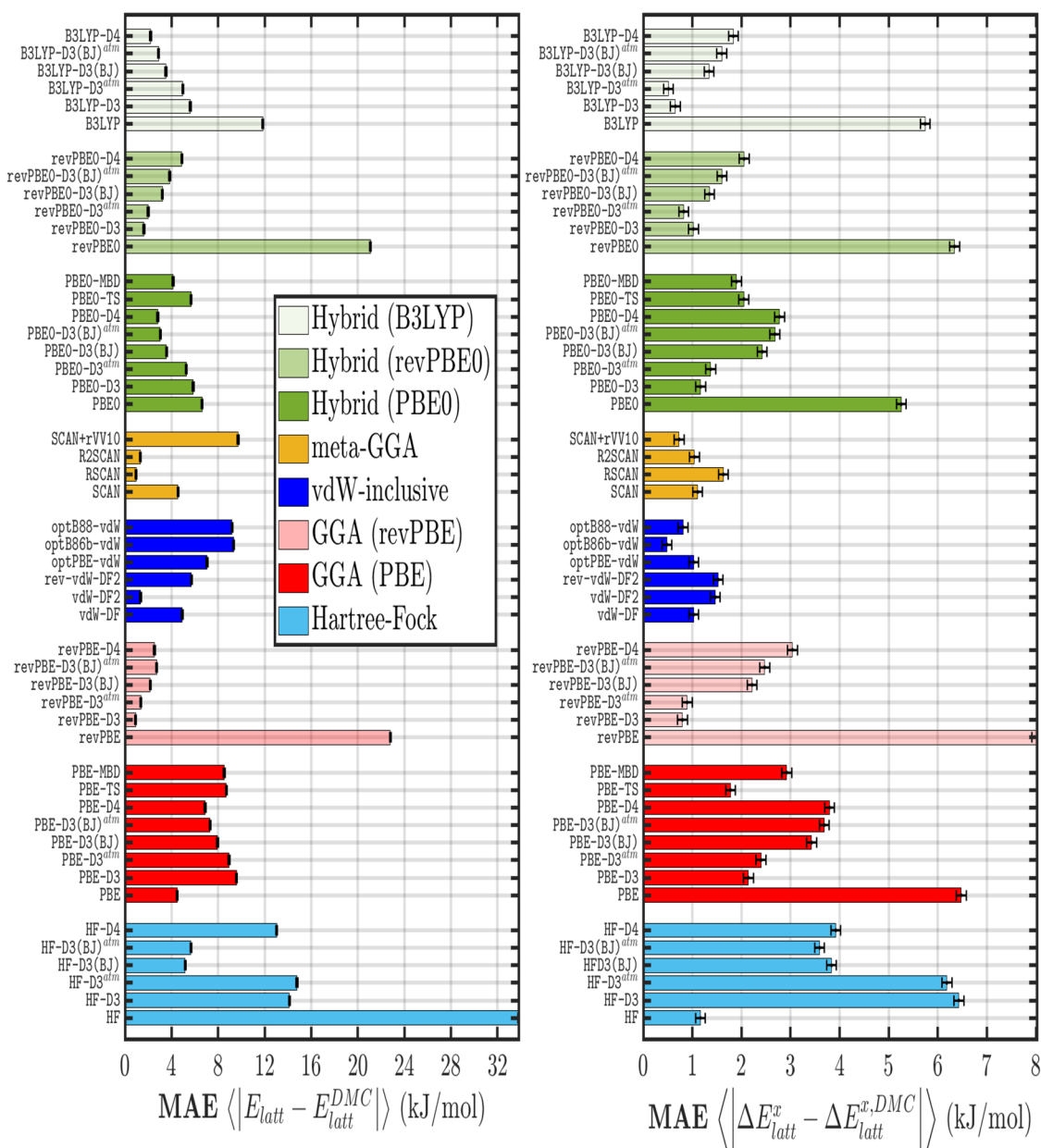
FIG. 3. Outcome of the benchmark, reported as Mean Absolute Error (MAE) with respect to the reference DMC values (black error bars indicate the DMC statistical error) for the absolute (left) and relative (right) lattice energies. The XC functionals have been ordered according to Jacob's ladder as Generalized Gradient Approximation (red), non-local van der Waals inclusive functionals (blue), *meta*-GGA (ochre), and hybrid (green). Different shades are used within GGA and hybrid methods to differentiate the basis dispersion-less functional. Hartree–Fock (cyan) results are also reported.

transition pressure can be crudely estimated as

$$p_{\text{tr}} = -\frac{\Delta E_{\text{XIII−III}}^{\text{DMC}}}{\Delta V_{\text{XIII−III}}^{p=0}} \sim 0.48 \text{ GPa.} \qquad (3)$$

Therefore, even in this approximation, our DMC data allow for the prediction of a reasonable transition pressure.[11] Assuming that the difference $\Delta V_{\text{XIII−III}}^0$ does not change significantly with the XC functional, then the condition that a functional needs to satisfy to predict the stability of ice III is $\Delta E_{\text{XIII−III}}^{\text{XC}} \sim \Delta E_{\text{XIII−III}}^{\text{DMC}}$. As can be computed from Table II, none of the functionals considered in Refs. 14 and 15, i.e., SCAN, PBE0+D3, revPBE0+D3, and B3LYP+D3, satisfies this condition. Details of the used approximation are reported in the
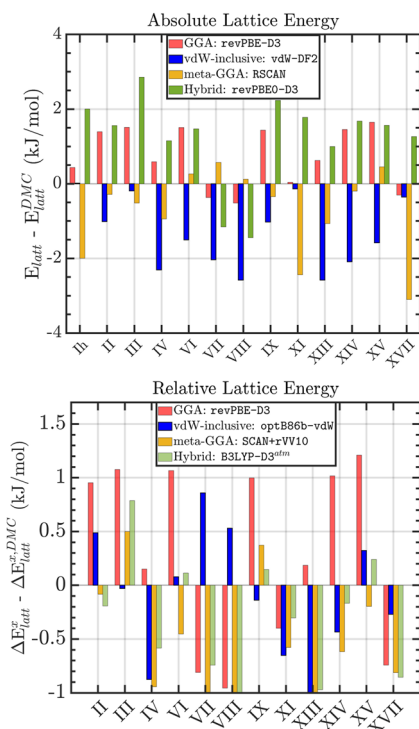
FIG. 4. Best performing DFT functional for each XC macro-class on the absolute (top) and relative (bottom) lattice energies. Each plot reports the difference between the DFT-XC and the reference DMC lattice energy for all the polymorphs in `DMC-ICE13`. Each XC functional bar is colored according to the color-map used in Fig. 3.

supplementary material, together with the performance of each XC functional on the transition pressure. Interestingly, none of the best performing functionals identified in our analysis captures this stability difference either.

Based on our benchmarks, it is clear that care should be taken when choosing which functional to use when computing a specific water-ice property. This conclusion is consistent with the recent work of Kapil et al.,[81] where it was shown that two different functionals, revPBE0-D3 and B3LYP-D3, perform better in capturing the vibrational spectrum of liquid water and hexagonal ice, respectively. From another perspective, despite the large amount of currently available DFT methods and the optimal (or sub-optimal) performance achieved by several of them, it is evident that there is still room for improvement, especially if we do not want to rely on error cancelation to reach the desired target.

Note also that, despite the large set of XC functionals tested, there are certainly other DFT methods that could be considered. In particular, the recently proposed Density-Corrected SCAN (DC-SCAN)[82,83] looks very promising, while the hybrid functional SCAN0[84] has been tested on liquid water showing better results than SCAN. Moving forward, it would be interesting to test these functionals, as well as others left outside this benchmark (e.g., numerous *meta*-GGAs or double hybrid functionals), on the `DMC-ICE13` set.

IV. CONCLUSION

We defined a set of 13 ice polymorphs, including both hydrogen-ordered and -disordered phases and ranging from low- to high-pressure phases. We computed absolute and relative lattice energies using DMC, which were shown to be always in excellent agreement (average error of ~0.5 kJ/mol) with available experimental data. Furthermore, our dataset allows us to qualitatively understand a discrepancy between the experimental and computational phase diagram, highlighting the significance of computing high-accuracy reference data. For polymorphs for which experimental lattice energies are not yet available, our DMC values serve as a useful reference against which new methods can be tested. Indeed, the fact that we can now compute 13 DMC lattice energies in a fairly rapid timescale underlines how DMC has become a powerful reference method for molecular crystals and condensed phase simulations with fairly large unit cells.

Here, we tested a broad range of DFT-XC functionals and, as seen in previous benchmarks, the performance of GGA and hybrid functionals generally improves when a dispersion correction is taken into account. Of the schemes considered, unreliable performance on the absolute lattice energies is achieved by HF (MAE > 30 kJ/mol) as well as by revPBE and revPBE0 (MAE ~ 20 kJ/mol). However, significant improvement is obtained with D3/D4 corrections for revPBE and revPBE0 (MAE < 5 kJ/mol). Almost equivalent performance is achieved by vdW-DF, PBE0+D, and B3LYP+D. The vdW-inclusive functionals generally offer good performance, this being particularly true for the relative lattice energies (MAE < 2 kJ/mol). Interestingly, the performance of an XC functional on the absolute and relative lattice energies can be significantly different, the most evident cases being HF, PBE, RSCAN, and PBE0. Indeed, it is clear from this work that ice phases define a challenging set for electronic structure methods, and that improvements are still needed to capture all its features with a single functional. Overall, our analysis suggests that revPBE-D3 and RSCAN (MAE ~ 0.9 kJ/mol) are the most accurate functionals for the absolute lattice energies, while optB86b-vdW and SCAN + rVV10 (MAE ~ 0.6 kJ/mol) are the best options, considering both accuracy and computational cost, for the relative lattice energies. Previous comparisons between water clusters and ice phases[21] suggested that these conclusions should be transferable to the liquid state, as well as to solid–water interfaces, where detailed benchmarks are hindered by the prohibitive computational cost.

SUPPLEMENTARY MATERIAL

See the supplementary material for the analyzes of the ice III–V phase transition and of the experimental estimates of the lattice energies, for details of our DMC and DFT simulations, and for the geometries considered in our dataset.

ACKNOWLEDGMENTS

AUTHOR DECLARATIONS

Conflict of Interest

The authors have no conflicts to disclose.

Author Contributions

Flaviano Della Pia: Conceptualization (equal); Data curation (equal); Formal analysis (equal); Writing – original draft (equal). **Andrea Zen**: Conceptualization (equal); Data curation (equal); Formal analysis (equal); Methodology (equal); Writing – review & editing (equal). **Dario Alfè**: Conceptualization (equal); Formal analysis (equal); Methodology (equal); Writing – review & editing (equal). **Angelos Michaelides**: Conceptualization (equal); Formal analysis (equal); Funding acquisition (equal); Project administration (equal); Resources (equal); Supervision (equal); Writing – review & editing (equal).

DATA AVAILABILITY

The data that support the findings of this study are available within the article and its supplementary material.

REFERENCES

[1] C. G. Salzmann, P. G. Radaelli, E. Mayer, and J. L. Finney, "Ice XV: A new thermodynamically stable phase of ice," Phys. Rev. Lett. **103**, 105701 (2009).

[2] A. Falenty, T. C. Hansen, and W. F. Kuhs, "Formation and properties of ice XVI obtained by emptying a type sII clathrate hydrate," Nature **516**, 231–233 (2014).

[3] L. del Rosso, F. Grazzi, M. Celli, D. Colognesi, V. Garcia-Sakai, and L. Ulivi, "Refined structure of metastable ice XVII from neutron diffraction measurements," J. Phys. Chem. C **120**, 26955–26959 (2016).

[4] M. Millot, F. Coppari, J. R. Rygg, A. Correa Barrios, S. Hamel, D. C. Swift, and J. H. Eggert, "Nanosecond x-ray diffraction of shock-compressed superionic water ice," Nature **569**, 251–255 (2019).

[5] C. G. Salzmann, J. S. Loveday, A. Rosu-Finsen, and C. L. Bull, "Structure and nature of ice XIX," Nat. Commun. **12**, 3162 (2021).

[6] E. A. Engel, A. Anelli, M. Ceriotti, C. J. Pickard, and R. J. Needs, "Mapping uncharted territory in ice from zeolite networks to ice structures," Nat. Commun. **9**, 2173 (2018).

[7] E. F. Burton and W. F. Oliver, "The crystal structure of ice at low temperatures," Proc. R. Soc. A **153**, 166–172 (1935).

[8] O. Mishima, L. D. Calvert, and E. Whalley, "'Melting ice' I at 77 k and 10 kbar: A new method of making amorphous solids," Nature **310**, 393–395 (1984).

[9] O. Mishima, L. D. Calvert, and E. Whalley, "An apparently first-order transition between two amorphous phases of ice induced by pressure," Nature **314**, 76–78 (1985).

[10] A. Rosu-Finsen, M. Davies, A. Amon, A. Sella, A. Michaelides, and C. Salzmann, "Medium-density amorphous ice," chemrxiv-2022-6ncg6 (2022).

[11] C. G. Salzmann, "Advances in the experimental exploration of water's phase diagram," J. Chem. Phys. **150**, 060901 (2019).

[12] C. McBride, E. G. Noya, J. L. Aragones, M. M. Conde, and C. Vega, "The phase diagram of water from quantum simulations," Phys. Chem. Chem. Phys. **14**, 10140–10146 (2012).

[13] S. L. Bore, P. M. Piaggi, R. Car, and F. Paesani, "Phase diagram of the TIP4p/Ice water model by enhanced sampling simulations," chemrxiv-2022-30cdf (2022).

[14] L. Zhang, H. Wang, R. Car, and E. Weinan, "Phase diagram of a deep potential water model," Phys. Rev. Lett. **126**, 236001 (2021).

[15] A. Reinhardt and B. Cheng, "Quantum-mechanical exploration of the phase diagram of water," Nat. Commun. **12**, 588 (2021).

[16] D. R. Hamann, "H_2O hydrogen bonding in density-functional theory," Phys. Rev. B **55**, R10157–R10160 (1997).

[17] P. J. Feibelman, "Lattice match in density functional calculations: Ice Ih vs β-AgI," Phys. Chem. Chem. Phys. **10**, 4688–4691 (2008).

[18] B. Santra, J. Klimeš, D. Alfè, A. Tkatchenko, B. Slater, A. Michaelides, R. Car, and M. Scheffler, "Hydrogen bonds and van der waals forces in ice at ambient and high pressures," Phys. Rev. Lett. **107**, 185701 (2011).

[19] B. Santra, J. Klimeš, A. Tkatchenko, D. Alfè, B. Slater, A. Michaelides, R. Car, and M. Scheffler, "On the accuracy of van der waals inclusive density-functional theory exchange-correlation functionals for ice at ambient and high pressures," J. Chem. Phys. **139**, 154702 (2013).

[20] Y. Fang, B. Xiao, J. Tao, J. Sun, and J. P. Perdew, "Ice phases under ambient and high pressure: Insights from density functional theory," Phys. Rev. B **87**, 214101 (2013).

[21] J. G. Brandenburg, T. Maas, and S. Grimme, "Benchmarking DFT and semiempirical methods on structures and lattice energies for ten ice polymorphs," J. Chem. Phys. **142**, 124104 (2015).

[22] J. Sun, R. C. Remsing, Y. Zhang, Z. Sun, A. Ruzsinszky, H. Peng, Z. Yang, A. Paul, U. Waghmare, X. Wu, M. L. Klein, and J. P. Perdew, "Accurate first-principles structures and energies of diversely bonded systems from an efficient density functional," Nat. Chem. **8**, 831–836 (2016).

[23] S. Jana, A. Patra, S. Śmiga, L. A. Constantin, and P. Samal, "Insights from the density functional performance of water and water–solid interactions: Scan in relation to other meta-GGAs," J. Chem. Phys. **153**(21), 214116 (2020).

[24] M. J. Gillan, D. Alfè, and A. Michaelides, "Perspective: How good is DFT for water?," J. Chem. Phys. **144**(13), 130901 (2016).

[25] E. Whalley, "Energies of the phases of ice at zero temperature and pressure," J. Chem. Phys. **81**, 4087 (1984).

[26] A. Zen, J. G. Brandenburg, J. Klimeš, A. Tkatchenko, D. Alfè, and A. Michaelides, "Fast and accurate quantum Monte Carlo for molecular crystals," Proc. Natl. Acad. Sci. U. S. A. **115**(8), 1724–1729 (2018).

[27] M. J. Gillan, D. Alfè, P. J. Bygrave, C. R. Taylor, and F. R. Manby, "Energy benchmarks for water clusters and ice structures from an embedded many-body expansion," J. Chem. Phys. **139**(11), 114101 (2013).

[28] M. Hellgren and L. Baguet, "Random phase approximation with exchange for an accurate description of crystalline polymorphism," Phys. Rev. Res. **3**, 033263 (2021).

[29] M. Macher, J. Klimeš, C. Franchini, and G. Kresse, "The random phase approximation applied to ice," J. Chem. Phys. **140**(8), 084502 (2014).

[30] Z. Raza, D. Alfè, C. G. Salzmann, J. Klimeš, A. Michaelides, and B. Slater, "Proton ordering in cubic ice and hexagonal ice; a potential new ice phase—XIc," Phys. Chem. Chem. Phys. **13**, 19788–19795 (2011).

[31] A. Zen, S. Sorella, M. J. Gillan, A. Michaelides, and D. Alfè, "Boosting the accuracy and speed of quantum Monte Carlo: Size consistency and time step," Phys. Rev. B **93**, 241118 (2016).

[32] A. Zen, J. G. Brandenburg, A. Michaelides, and D. Alfè, "A new scheme for fixed node diffusion quantum Monte Carlo with pseudopotentials: Improving reproducibility and reducing the trial-wave-function bias," J. Chem. Phys. **151**, 134105 (2019).

[33] K. Momma and F. Izumi, "VESTA3 for three-dimensional visualization of crystal, volumetric and morphology data," J. Appl. Crystallogr. **44**(6), 1272–1276 (2011).

[34]S. Nanayakkara, Y. Tao, and E. Kraka, "Capturing individual hydrogen bond strengths in ices via periodic local vibrational mode theory: Beyond the lattice energy picture," J. Chem. Theory Comput. **18**, 562–579 (2022).

[35]G. Kresse and J. Hafner, "*Ab initio* molecular dynamics for liquid metals," Phys. Rev. B **47**, 558 (1993).

[36]G. Kresse and J. Hafner, "*Ab initio* molecular-dynamics simulation of the liquid-metal–amorphous-semiconductor transition in germanium," Phys. Rev. B **49**, 14251 (1994).

[37]G. Kresse and J. Furthmüller, "Efficiency of ab-initio total energy calculations for metals and semiconductors using a plane-wave basis set," Comput. Mater. Sci. **6**, 15 (1996).

[38]G. Kresse and J. Furthmüller, "Efficient iterative schemes for *ab initio* total-energy calculations using a plane-wave basis set," Phys. Rev. B **54**, 11169 (1996).

[39]G. Kresse and D. Joubert, "From ultrasoft pseudopotentials to the projector augmented-wave method," Phys. Rev. B **59**, 1758 (1999).

[40]P. E. Blöchl, "Projector augmented-wave method," Phys. Rev. B **50**, 17953 (1994).

[41]H. Partridge and D. W. Schwenke, "The determination of an accurate isotope dependent potential energy surface for water from extensive ab initio calculations and experimental data," J. Chem. Phys. **106**(11), 4618–4639 (1997).

[42]J. G. Brandenburg, A. Zen, D. Alfè, and A. Michaelides, "Interaction between water and carbon nanostructures: How good are current density functional approximations?," J. Chem. Phys. **151**(16), 164702 (2019).

[43]J. P. Perdew and A. Zunger, "Self-interaction correction to density-functional approximations for many-electron systems," Phys. Rev. B **23**, 5048–5079 (1981).

[44]J. P. Perdew, K. Burke, and M. Ernzerhof, "Generalized gradient approximation made simple," Phys. Rev. Lett. **77**, 3865–3868 (1996).

[45]Y. Zhang and W. Yang, "Comment on 'generalized gradient approximation made simple,'" Phys. Rev. Lett. **80**, 890 (1998).

[46]J. Klimeš, D. R. Bowler, and A. Michaelides, "Chemical accuracy for the van der waals density functional," J. Phys.: Condens. Matter **22**(2), 022201 (2009).

[47]J. Klimeš, D. R. Bowler, and A. Michaelides, "Van der waals density functionals applied to solids," Phys. Rev. B **83**, 195131 (2011).

[48]M. Dion, H. Rydberg, E. Schröder, D. C. Langreth, and B. I. Lundqvist, "Van der waals density functional for general geometries," Phys. Rev. Lett. **92**, 246401 (2004).

[49]K. Lee, E. D. Murray, L. Kong, B. I. Lundqvist, and D. C. Langreth, "Higher-accuracy van der waals density functional," Phys. Rev. B **82**, 081101 (2010).

[50]I. Hamada, "Van der waals density functional made accurate," Phys. Rev. B **89**, 121103 (2014).

[51]J. Sun, A. Ruzsinszky, and J. P. Perdew, "Strongly constrained and appropriately normed semilocal density functional," Phys. Rev. Lett. **115**, 036402 (2015).

[52]A. P. Bartók and J. R. Yates, "Regularized scan functional," J. Chem. Phys. **150**(16), 161101 (2019).

[53]J. W. Furness, A. D. Kaplan, J. Ning, J. P. Perdew, and J. Sun, "Accurate and numerically efficient r2SCAN meta-generalized gradient approximation," J. Phys. Chem. Lett. **11**(19), 8208–8215 (2020).

[54]H. Peng, Z.-H. Yang, J. P. Perdew, and J. Sun, "Versatile van der waals density functional based on a meta-generalized gradient approximation," Phys. Rev. X **6**, 041005 (2016).

[55]J. P. Perdew, M. Ernzerhof, and K. Burke, "Rationale for mixing exact exchange with density functional approximations," J. Chem. Phys. **105**(22), 9982–9985 (1996).

[56]C. Adamo and V. Barone, "Toward reliable density functional methods without adjustable parameters: The PBE0 model," J. Chem. Phys. **110**(13), 6158–6170 (1999).

[57]L. Goerigk and S. Grimme, "A thorough benchmark of density functional methods for general main group thermochemistry, kinetics, and noncovalent interactions," Phys. Chem. Chem. Phys. **13**, 6670–6688 (2011).

[58]A. D. Becke, "Density-functional thermochemistry. III. The role of exact exchange," J. Chem. Phys. **98**(7), 5648–5652 (1993).

[59]C. Lee, W. Yang, and R. G. Parr, "Development of the Colle–Salvetti correlation-energy formula into a functional of the electron density," Phys. Rev. B **37**, 785–789 (1988).

[60]S. Grimme, J. Antony, S. Ehrlich, and H. Krieg, "A consistent and accurate *ab initio* parametrization of density functional dispersion correction (DFT-D) for the 94 elements H-Pu," J. Chem. Phys. **132**, 154104 (2010).

[61]S. Grimme, S. Ehrlich, and L. Goerigk, "Effect of the damping function in dispersion corrected density functional theory," J. Comput. Chem. **32**(7), 1456–1465 (2011).

[62]E. Caldeweyher, C. Bannwarth, and S. Grimme, "Extension of the D3 dispersion coefficient model," J. Chem. Phys. **147**(3), 034112 (2017).

[63]E. Caldeweyher, S. Ehlert, A. Hansen, H. Neugebauer, S. Spicher, C. Bannwarth, and S. Grimme, "A generally applicable atomic-charge dependent london dispersion correction," J. Chem. Phys. **150**(15), 154122 (2019).

[64]E. Caldeweyher, J.-M. Mewes, S. Ehlert, and S. Grimme, "Extension and evaluation of the D4 london-dispersion model for periodic systems," Phys. Chem. Chem. Phys. **22**, 8499–8512 (2020).

[65]A. Tkatchenko and M. Scheffler, "Accurate molecular van der waals interactions from ground-state electron density and free-atom reference data," Phys. Rev. Lett. **102**, 073005 (2009).

[66]A. Tkatchenko, R. A. DiStasio, R. Car, and M. Scheffler, "Accurate and efficient method for many-body van der waals interactions," Phys. Rev. Lett. **108**, 236402 (2012).

[67]A. Ambrosetti, A. M. Reilly, R. A. DiStasio, and A. Tkatchenko, "Long-range correlation energy calculated from coupled atomic response functions," J. Chem. Phys. **140**(18), 18A508 (2014).

[68]R. J. Needs, M. Towler, N. Drummond, P. López Ríos, and J. Trail, "Variational and diffusion quantum Monte Carlo calculations with the casino code," J. Chem. Phys. **152**, 154106 (2020).

[69]J. R. Trail and R. J. Needs, "Erratum: "smooth relativistic Hartree-Fock pseudopotentials for H to Ba and Lu to Hg" [J. Chem. Phys. 122, 174109 (2005)]," J. Chem. Phys. **139**(3), 039902 (2013).

[70]J. R. Trail and R. J. Needs, "Norm-conserving Hartree–Fock pseudopotentials and their asymptotic behavior," J. Chem. Phys. **122**(1), 014112 (2005).

[71]See http://www.quantum-espresso.org./ for more information about Quantum espresso.

[72]See http://www.pwscf.org./ for more information about Pwscf.

[73]D. Alfè and M. J. Gillan, "Efficient localized basis set for quantum Monte Carlo calculations on condensed matter," Phys. Rev. B **70**, 161101 (2004).

[74]W. M. C. Foulkes, L. Mitas, R. J. Needs, and G. Rajagopal, "Quantum Monte Carlo simulations of solids," Rev. Mod. Phys. **73**, 33–83 (2001).

[75]L. Fraser, W. Foulkes, G. Rajagopal, R. Needs, S. Kenny, and A. Williamson, "Finite-size effects and Coulomb interactions in quantum Monte Carlo calculations for homogeneous systems with periodic boundary conditions," Phys. Rev. B **53**, 1814–1832 (1996).

[76]A. Williamson, G. Rajagopal, R. Needs, L. Fraser, W. Foulkes, Y. Wang, and M.-Y. Chou, "Elimination of Coulomb finite-size effects in quantum many-body simulations," Phys. Rev. B **55**, R4851 (1997).

[77]P. R. C. Kent, R. Q. Hood, A. J. Williamson, R. J. Needs, W. M. C. Foulkes, and G. Rajagopal, "Finite-size errors in quantum many-body simulations of extended systems," Phys. Rev. B **59**, 1917–1929 (1999).

[78]C. Lin, F. H. Zong, and D. M. Ceperley, "Twist-averaged boundary conditions in continuum quantum Monte Carlo algorithms," Phys. Rev. E **64**, 016702 (2001).

[79]M. Chen, H.-Y. Ko, R. C. Remsing, M. F. C. Andrade, B. Santra, Z. Sun, A. Selloni, R. Car, M. L. Klein, J. P. Perdew, and X. Wu, "Ab initio theory and modeling of water," Proc. Natl. Acad. Sci. U. S. A. **114**(41), 10846–10851 (2017).

[80]P. M. Piaggi, A. Z. Panagiotopoulos, P. G. Debenedetti, and R. Car, "Phase equilibrium of water with hexagonal and cubic ice using the scan functional," J. Chem. Theory Comput. **17**(5), 3065–3077 (2021).

[81]V. Kapil, D. M. Wilkins, J. Lan, and M. Ceriotti, "Inexpensive modeling of quantum dynamics using path integral generalized Langevin equation thermostats," J. Chem. Phys. **152**(12), 124104 (2020).

[82]S. Dasgupta, E. Lambros, J. P. Perdew, and F. Paesani, "Elevating density functional theory to chemical accuracy for water simulations through a density-corrected many-body formalism," Nat. Commun. **12**, 6359 (2021).

[83]S. Dasgupta, S. Chandra, B. Pradeep, J. P. Perdew, and F. Paesani, "How good is the density-corrected scan functional for neutral and ionic aqueous systems, and what is so right about the Hartree-Fock density?," chemrxiv-2022-8r5v9 (2022).

[84]C. Zhang, F. Tang, M. Chen, J. Xu, L. Zhang, D. Y. Qiu, J. P. Perdew, M. L. Klein, and X. Wu, "Modeling liquid water by climbing up Jacob's ladder in density functional theory facilitated by using deep neural network potentials," J. Phys. Chem. B **125**(41), 11444–11456 (2021).